Applied Catalysis B: Environmental 286 (2021) 119897

Contents lists available at ScienceDirect

Applied Catalysis B: Environmental

journal homepage: www.elsevier.com/locate/apcatb

Fe and P Doped 1T-Phase Enriched $WS_2$3D-Dendritic Nanostructures for Efficient Overall Water Splitting

Dasu Ram Paudel [a,b], Uday Narayan Pan [a], Thangjam Ibomcha Singh [a], Chandan Chandru Gudal [a], Nam Hoon Kim [a,*], Joong Hee Lee [a,c,*]

[a] Department of Nano Convergence Engineering (BK21 Four), Jeonbuk National University, Jeonju, Jeonbuk, 54896, Republic of Korea
[b] Department of Chemistry, Tri-Chandra Multiple Campus, Tribhuvan University, Kathmandu, 44613, Nepal
[c] Carbon Composite Research Centre, Jeonbuk National University, Jeonju, Jeonbuk, 54896, Republic of Korea

ARTICLE INFO

Keywords:
1T-WS_2
Active basal plane
3D-dendritic nanostructure
Water splitting
HER
OER

ABSTRACT

1T-WS_2 is known for its higher hydrogen evolution reaction (HER) performance than 2H-WS_2. However, the lack of thermodynamic stability and absence of large-scale synthesis procedures kept 1T-WS_2 significantly ignored to date. In this report, for the first time, we have fabricated 1T-WS_2 in 3D-dendritic nanostructures over flexible carbon cloth (CC) following doping and intercalation of Fe and P (1T-Fe/P-WS_2@CC). The HER and OER activities of 1T-Fe/P-WS_2@CC outperform state-of-the-art electrocatalysts, demonstrating a low overpotential (η_{HER} =116 mV, η_{OER} =267 mV @ 10 mA cm^{-2}), small Tafel slope (HER =65 mV dec^{-1}, OER =70.1 mV dec^{-1}), and significant durability. The 1T-Fe/P-WS_2@CC (+,−) alkaline elctrolyzer also shows exceptional high performance, required only 1.53 V cell voltage at the current density of 10 mA cm^{-2}. Overall, this work opens up a new dimension for simple and scalable fabrication of highly efficient and low-cost electrocatalyst based on WS_2.

1. Introduction

With the significant increase in environmental pollution and global warming as a direct result of the uncontrolled fossil fuels consumption over the last decade, there is an urgent need to find viable ways to utilize renewable energy resources on an industrial scale to achieve zero-emission energy feasibility [1–4]. Regarding this, electrocatalytic water splitting (EWS) is recognized as one of the most promising way to generate green hydrogen (H_2) fuel [5–7]. EWS is basically a combination of two half reactions, the cathodic half reaction is commonly known as the hydrogen evolution reaction (HER) and the anodic half reaction is commonly known as oxygen evolution reaction (OER) [6,8,9]. In EWS, electrocatalysts play the most critical role by reducing the required activation energy for HER and OER reaction to achieve cost practicality [5,9,10]. To date, noble-metal based catalysts, like, platinum (Pt) for HER and iridium oxide (IrO_2) and ruthenium oxide (RuO_2) for OER is considered as the most efficient electrocatalysts, however, their scarcity and high cost caused low economic appeal [6,11]. Therefore, development of earth abundant material based electrocatalysts with competitive activity and long-term stability is desirable for economic viability of the technique [3,5,9,12].

Transition metal dichalcogenides (TMDCs) have attracted a lot of attention as electrocatalyst for EWS due to their high abundancy, excellent chemical stability, intrinsic semiconducting characteristics, and high catalytic efficacy [8,13–17]. Among various TMDCs, recently, much attention has been paid to tungsten disulfide (WS_2) due to its excellent physical and chemical stabilities, multiple oxidation states, high melting temperatures, and robust mechanical properties [18–21]. WS_2 is composed of multilayered nanosheets creates polymorphism with unique phases like 2H (D_{3h}, semiconducting), 3R (C^5_{3v}, semiconducting) and 1T (O_h, metallic) [22]. So far, most researchers have considered 2H-WS_2 for EWS owing to its high thermodynamic stability and ease of synthesis [21–24]. However, 1T-WS_2 shows much higher catalytic efficacy due to its lower band gap, high density of active sites on the basal planes, tailored exposed edge sites, and S—WS— octahedral coordination compared to the 2H or 3R-phases. But, lack of thermodynamic stability and difficulties in large scale synthesis have kept 1T-WS_2 significantly ignored for EWS till date [19,25,26]. Nevertheless, many recent reports indicated that the doping and intercalation of different transition metals and nonmetals is capable of introducing higher thermodynamic stability to 1T-WS_2 along with high yielding synthesis methods [14,25–27]. Doping elements basically generates crystal strain

* Corresponding authors at: Department of Nano Convergence Engineering (BK21 Four), Jeonbuk National University, Jeonju, Jeonbuk, 54896, Republic of Korea.
E-mail addresses: nhk@jbnu.ac.kr (N.H. Kim), jhl@jbnu.ac.kr (J.H. Lee).

https://doi.org/10.1016/j.apcatb.2021.119897
Received 15 November 2020; Received in revised form 24 December 2020; Accepted 3 January 2021
Available online 13 January 2021

in the seeds of the WS_2 formed during the very early state of the reaction in the bottom-up approach and alters the growth mechanism to form 1T-WS_2 [14,28]. Moreover, in many recent theoretical and experimental reports it has been shown that the doping of transition metals like Fe, Ni, Co, and V increase the electron density around the metal centers while the anions like P, N, and B effectively strengthens chemical bonding to promote chemical stability and catalytic durability and also activates the basal planes along with increased interlayer spacing [14,16,29–31]. The electron donating characteristic of the alkali or transition metal to the host phase of WS_2 together with the possibility of crystallographic strain generation following intercalation and doping of the nonmetal of larger size than S has been proposed as a possible route for stabilization of the 1T-phase of WS_2 [19,32]. It has also been depicted that doping of the heteroatom with different radiuses enhance the intrinsic conductivity of pristine WS_2 along with generating active centers for OER, thus, introduces bifunctionality to the catalyst [14,31]. Apart from improving intrinsic behavior, doping also plays a very crucial role in shape engineering of the nanostructures by leading to viable bond formation possibilities between similar and dissimilar elements [13,14]. Simultaneous doping of multiple elements holds the possibilities of generating better nanostructures with higher surface area porosity and electrochemically active sites [14,33]. Thus, it can be concluded that simultaneous doping and intercalation of multiple elements on WS_2 can boosts the catalytic efficacy of it for EWS by significantly improving the intrinsic characteristics like conductivity, density of active sites on the basal planes, expansion of interlayers, generation of additional active sites, manipulation of electron density around the metal atoms and also by improving physical characteristics like surface area and porosity.

Herein, we report fabrication of agave-leave type 3D-dendritic nanostructures of iron and phosphorus co-intercalated and doped 1T-enriched tungsten disulphide (WS_2) on flexible carbon cloth substrate as highly efficient electrocatalysts for overall water splitting. In this work, we have combined all the possible factors which are known for improving the catalytic efficacy of WS_2, namely, enrichment of 1T-phase for improving conductivity, activating latent basal planes for increasing density of the catalytically active sites and generation of highly porous nanostructures with high surface area in a single system for the first time to achieve uppermost catalytic water splitting efficacy of WS_2. Although it is difficult to determine which factor plays a predominant role exactly or which factors intertwine or influence each other significantly, simultaneous doping and intercalation of Fe and P helps in enrichment of 1T-phase of WS_2 and in increasing active sites for catalysis as active basal planes and thus boosts the HER performance. Fe-doping helps in generating OER active sites thus, transform OER inactive WS_2 to a bifunctional electrocatalyst. Moreover, doping of Fe and P played a crucial role in tailoring the morphology for generating agave-leave type 3D-dendritic nanostructure of 1T-WS_2 with very high surface area and porosity that in tandem with the improvement in the intrinsic properties plays significant role in boosting both HER and OER catalytic efficacy of WS_2 toward the highest possible limit.

2. Experimental details

2.1. Chemicals

Carbon cloth (CC) was purchased from Nara Cell-Tech (W0S1002). Sodium hypophosphite monohydrate ($NaH_2PO_2.H_2O$; ≥99.0 %), potassium hydroxide (KOH; ACS reagent, ≥85.0 %, Pellets), sodium tungstate dihydrate ($Na_2WO_4.2H_2O$; ACS reagent, ≥99.0 %), thiourea ($(NH_2)_2CS$; ACS reagent, ≥99.0 %), hydroxylamine hydrochloride ($NH_2OH.HCl$; ACS reagent, 98.0 %), ferric nitrate nonahydrate ($Fe(NO_3)_3{\cdot}9H_2O$; ≥99.95 % trace metal basis), Pt/C (10 wt. % loading), ruthenium (IV) oxide (99.9 % trace metal basis) were purchased from Sigma – Aldrich Co. All the chemicals were used without any additional cleansing.

2.2. Materials fabrication

2.2.1. Cleaning of carbon cloth (CC)

For cleaning the carbon cloths (CC), CCs of size 2 × 5 cm^2 was pretreated by refluxing in concentrated HNO_3 at 70 °C for about 4 h to remove impurities from the surface and for improving the hydrophilicity. Then the unreacted acids from the CCs were removed following ultrasonication in the presence of acetone, deionized water, and alcohol in sequence and finally dried in air and kept for future use.

2.2.2. Synthesis of Fe and P doped 3D-dendritic nanostructures of 1T-WS_2 on carbon cloth (1T-Fe/P-WS_2@CC)

For the synthesis of 1T-Fe/P-WS_2@CC, 1 mM sodium tungstate dihydrate ($Na_2WO_4.2H_2O$), 1 mM of sodium hypophosphite monohydrate ($NaH_2PO_2.H_2O$), 6 mM thiourea (NH_2CSNH_2) and 2 mM hydroxylamine hydrochloride ($NH_2OH.HCl$) were dissolved in 25 mL DI water by gentle magnetic stirring for 30 min to attain a clear solution. Then 0.2 mM ferric nitrate nonahydrate ($Fe(NO_3)_3{\cdot}9H_2O$) was dissolved in 25 mL DI water separately and then added dropwise into the first mixture solution under magnetic stirring. The mixture was then relocated to a 100 mL teflon-lined autoclave loaded with a piece of 2 × 5 cm^2 CC supported with glass slides and continued under 190 °C for 14 h. Once the reaction finished, 1T-Fe/P-WS_2@CC was prudently cleaned with ethanol and water mixture and then dehydrated in a vacuum oven overnight and kept for further use.

2.2.3. Synthesis of control materials

The hydrothermal reaction was conducted in a similar way for the preparation of tungsten sulphide nanostructures on CC (WS_2@CC), iron doped tungsten sulphide nanostructures on CC (Fe-WS_2@CC) and phosphorus doped tungsten sulphide nanostructures on CC (P-WS_2@CC). For this, the respective precursor salts were mixed in the desired molar ratios and subsequently heated to 190 °C for 14 h and dried in vacuum oven at 60 °C for overnight.

2.2.4. Preparation of Pt/C and RuO_2 based working electrode on CC

To compare the performance of the as synthesized materials, reference electrodes were prepared. For the HER, a Pt/C based electrode was prepared on CC. To do this, first Pt/C ink was made by dispersing 10 mg of platinum on carbon (10 wt.%) catalyst into 950 μL of water/isopropyl alcohol (v/v = 1:5), 50 μL of 5 wt.% nafion was also added to the solution which was then mixed by sonication for 30 min. Then, the Pt/C ink was drop casted onto the surface of bare CC with a 1 × 1 cm^2 geometric area before being dried out completely in a vacuum oven at 60 °C. Similarly, for the OER, RuO_2 ink was prepared by dispersing 10 mg of Ruthenium (IV) Oxide (99.9 % trace metal basis) catalyst into 950 μL of water/isopropyl alcohol (v/v = 1:5), 50 μL of 5 wt.% nafion was also added to the solution which was then mixed following sonication for 30 min. Then, the RuO_2 ink was loaded onto bare CC with a 1 × 1 cm^2 geometric area and dried out.

2.3. Structural characterization

The morphological, crystallographic and elemental composition of the 1T-Fe/P-WS_2@CC, WS_2@CC, Fe-WS_2@CC, and P-WS_2@CC were analyzed by transmission electron microscope (TEM, Model: JEM-2200FS instrument JEOL Co., USA). Selected area electron diffraction (SAED) pattern and elemental composition from energy dispersive X-ray (EDX) spectroscopy were obtained using the same TEM machine at a hastening voltage of 200 kV. Field emission scanning electron microscope (FE-SEM, Model: Supra 40 V P instrument Zeiss Co., Germany) were used to obtain the FESEM images and energy dispersive X-ray spectroscopy (EDS) based elemental composition in the Center for University-Wide Research Facilities (CURF) of Jeonbuk National University. X-ray diffraction (XRD) patterns were obtained using X-ray diffraction meter (Model: D/Max 2500 V/PC; Rigaku Co., Japan) to

identify the phase of the nanomaterials. The XRD patterns of the samples were obtained using a Cu target Kα X-ray (λ =0.154 nm) radiations in 2θ range of 8 – 80° at a scan rate of 2° min^{-1}. X-ray photoelectron spectroscopic (XPS) data was obtained using VG ESCALAB 220i spectrometer at KBSI of Jeonju Center. Raman spectroscopy data was obtained using Renishaw confocal microscope-based Raman spectrometer. 532 nm laser excitation was used of laser power 0.2 mW.

2.4. Electrochemical characterization

All electrochemical measurements were carried out using a CHI660E electrochemical workstation (CH Instruments, Inc., USA). The Ag/AgCl electrode dipped in 3.0 M L^{-1} KCl were used as the reference electrode and a graphite rod as counter electrode. Double-layer capacitance (C_{dl}), electrochemical surface area (ECSA) were measured using CV scans at multiple scan rates from 10 - 100 mV s^{-1} in non-faradic regions.

2.5. Preparation of electrolyte

For the preparation of the N_2-saturated 1 M KOH, 2.8 g of KOH pellets were dissolved in water to prepare a solution of 50 mL 1 M KOH. Then the solution was purged with N2-gas for 15 min to prepare N_2-saturated 1 M KOH used as an electrolyte for electrochemical measurements.

2.6. Calculation of potential vs. RHE

The obtained potential was transformed to reversible hydrogen electrode (RHE) potential following the equation below.

$$E_{RHE} = E_{Ag/AgCl} + 0.0591\ pH + E^{\circ}_{Ag/AgCl} \quad (1)$$

2.7. iR correction

The iR correction was carried out using the following equation

$$E_{Corrected} = E_{RHE} - iR_s \quad (2)$$

where i = current and R_s = equivalent series resistance.

2.8. Tafel slope

The Tafel slope is calculated following the equation

$$\eta = a + b \log j \quad (3)$$

where η= overpotential, b = Tafel slope, j= current density, and a = constant.

2.9. Electrochemically active surface area (ECSA)

The electrochemically active surface area (ECSA) was calculated by using the following equation.

$$ECSA = \frac{Double\ layer\ capacitance\ (Cdl)}{Cs} \quad (4)$$

where Cs is the specific capacitance of a flat surface.

3. Results and discussion

The iron and phosphorus doped and co-intercalated 1T-enriched tungsten disulphide on carbon cloth (*1T-Fe/P-WS_2@CC*) was prepared by a single step hydrothermal reaction. The precursor salts were first mixed in the desired proportions, a clean carbon cloth (CC) was then dipped into it and then the reaction mixture was incubated at 190 ℃ for 14 h (Scheme 1, more detail in experimental section). This one-pot synthetic strategy suits the large-scale fabrication of the electrodes at low cost making for the fabrication of *1T-Fe/P-WS_2@CC* industrially viable [24,34,35]. The doping and intercalation of Fe and P helps in the enrichment of the 1T-phase and in tandem activate the basal planes and improve the morphology thereby, improves catalytic efficacy significantly [25,36].

3.1. Morphological and crystallographic characterization

To explore the morphology of the as synthesized *1T-Fe/P-WS_2@CC*, the typical field emission scanning electron microscopic (FE-SEM) and transmission electron microscopic (TEM) images were examined, and the results were represented in Fig. 1. The FE-SEM images showed an agave-leave type 3D-dendritic nanostructure (Fig. 1**A-B**) of the as-prepared *1T-Fe/P-WS_2@CC*. The nanostructures are uniform in nature having hinged flakes and vertically grafted on a carbon cloth substrate with around 100−200 nm in vertical length. The high-magnification FE-SEM image (Fig. 1C) further reveals that the edges and the surface of the dendritic nanostructures are rough, which increases the overall surface area of the catalyst. The precise structural examination of *1T-Fe/P-WS_2@CC* by transmission electron microscopic (TEM; Fig. 1**D-E**) images and high-resolution transmission electron microscopic (HRTEM; Fig. 1**F**) images showed consistency with the FESEM images. Moreover, TEM images also revealed ripples and corrugations nature of the ultrathin 3D-dendritic nanostructures indicating high flexibility and large surface area [37,38]. The marked lattice pitch of several layers confirmed

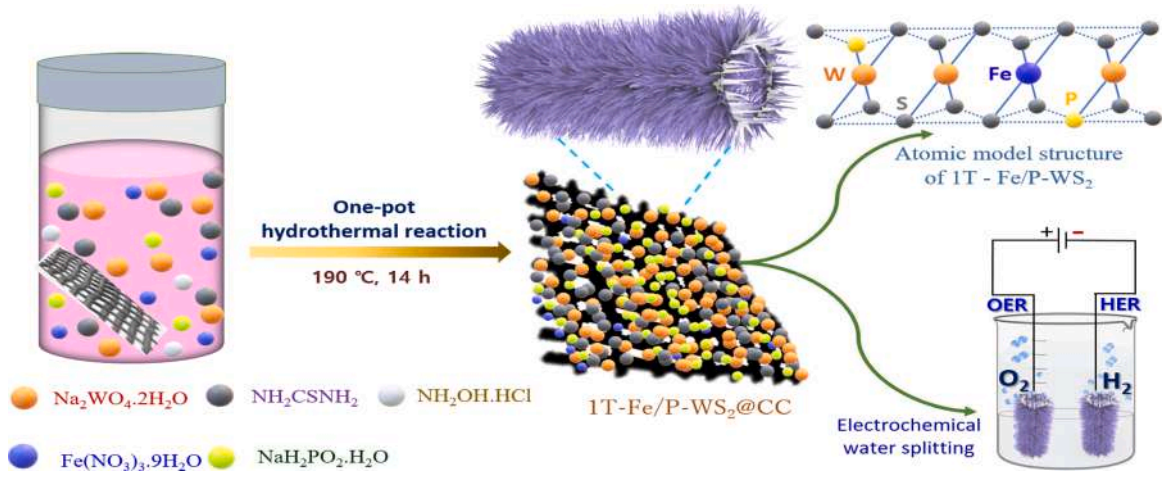

Scheme 1. Schematic representation of the fabrication of *1T-Fe/P-WS_2@CC* for electro-catalytic water-splitting (EWS).

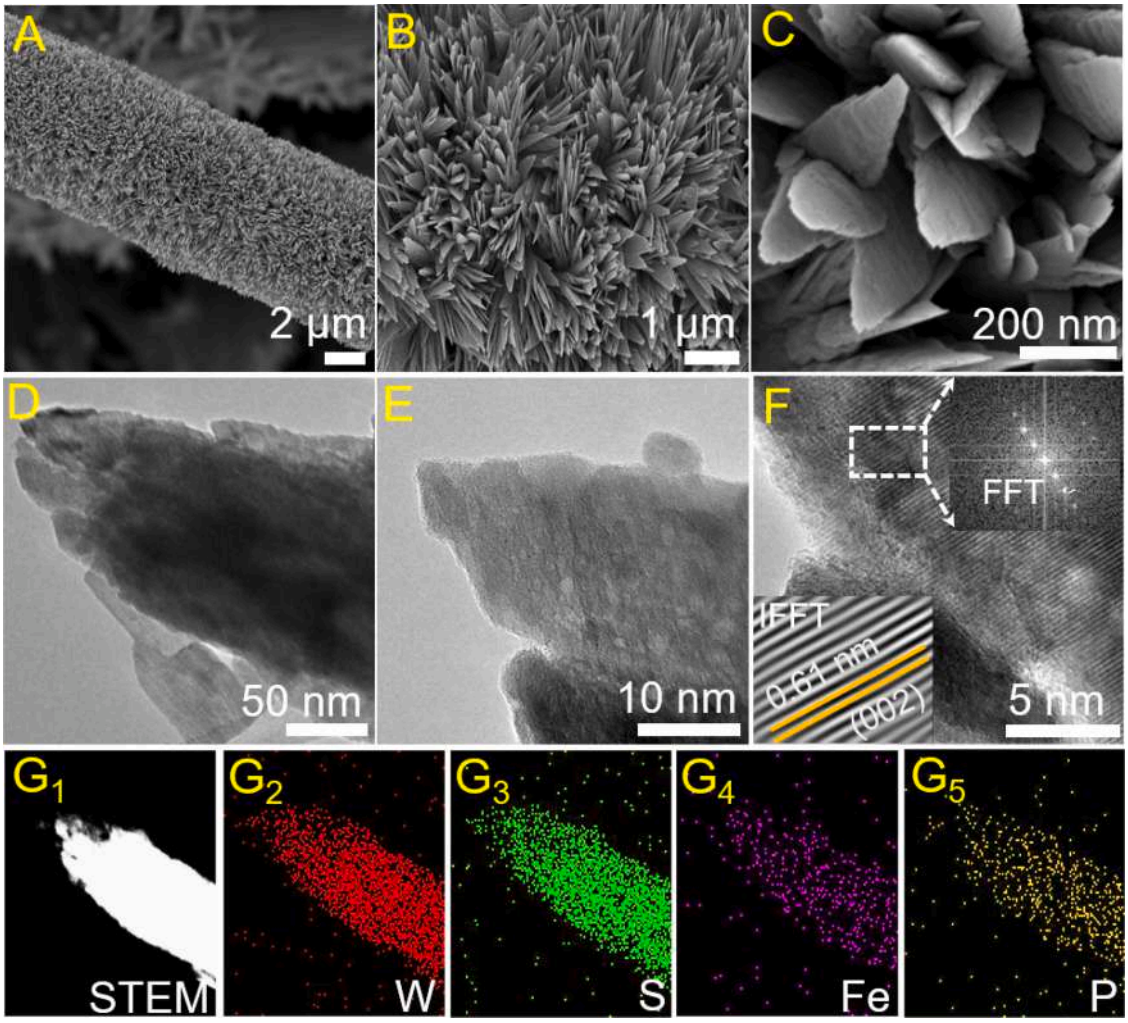

Fig. 1. (A–C) FE-SEM images at different magnifications (low to high) of 1T-Fe/P-WS_2@CC, showing the ultrathin 3D-dendritic nanostructures. (D-E) TEM image of 1T- Fe/P-WS_2@CC. (F) HRTEM image and corresponding fast Fourier transform (FFT) and inverse fast Fourier transform (IFFT) pattern (inset) of 1T- Fe/P-WS_2@CC (G_1) STEM image and corresponding elemental mapping of 1T- Fe/P-WS_2@CC showing the presence of individual constituent elements: (G_2) Tungsten (W), (G_3) Sulphur (S), (G_4) Iron (Fe), and (G_5) Phosphorus (P).

following fast Fourier transform (FFT) and inverse fast Fourier transform (IFFT) images are dominated by well-defined crystalline edges (Fig. 1F) which matches with the (002) plane of the *1T-Fe/P-WS_2@CC* confirming the formation of the same [23,31,36]. Scanning transmission electron microscopy (STEM) (Fig. 1**G_1**) and energy dispersive X-ray (EDX) color mapping (Fig. 1, **G_2-G_5**) analysis was performed for the validation of the elemental composition of the material, results showed all the elements i. e. W, Fe, S, and P are present in homogeneous distribution in equivalent amount indicating formation of the desire material. The energy dispersive spectroscopy (EDS) elemental mapping analysis obtained from FE-SEM also showed the similar results like TEM-EDX (**Figure S1**, Supporting Information), EDX spectrum and corresponding elemental distribution of all constituent elements in color mapping over CC clearly confirms the Fe and P doping on WS_2 **(Figure S1,** supporting information**)**. Atomic resolution TEM image of *1T-Fe/P-WS_2@CC* (**Figure S2,** supporting information) confirms the formation of the 1T-pahse and the presence of the dopants element in the lattice [25,28]. Further confirmation of the elemental composition was also performed using Inductively Coupled Plasma Atomic Emission Spectroscopy (ICP-OES) to correlate the elemental composition with EDX showing the presence of the element in 27.1 % (W), 58.9 % (S), 7.2 % (Fe) and 6.8 % (P) (**Table S1,** supporting information). The FESEM images of the WS_2@CC prepared in the similar set of conditions also revealed the sheet structure (Fig. 2A–C) but the length of the sheet is much smaller compared to the *1T-Fe/P-WS_2@CC*(Figs. 1A and 2 A**)**. WS_2 nanosheets changed into the nanoflakes like morphology when P doping was carried out (Fig. 2D–F). But the structure of the P-WS_2@CC are not uniform and bland type indicating possibility of having low surface area. The iron doping on WS_2 lead to growth small nano threads like structure (Fig. 2G–I) which are uniform but looks inferior compared to *1T-Fe/P-WS_2@CC* in terms of surface area. The surface area and porosity measurement also supported the conclusion obtained from FE-SEM results. The surface areas and porosity were measured following nitrogen adsorption-desorption study conducted at 77 K and calculated using Brunauer-Emmette-Teller (BET) isotherms and Barrett-Joyner-Halenda (BJH) pore size distribution. All the samples showed characteristic type IV Brunauer-Deming-Deming-Teller (BDDT) isotherms (Fig. 3A) indicating the homogeneity of bimodal pore distribution in the mesoporous regions. The BET surface area of the as synthesized 1T-Fe/P-WS_2@CC sample was obtained 79 $m^2\ g^{-1}$, which is found to be much higher than that of the WS_2@CC (36 $m^2\ g^{-1}$), P-WS_2@CC (25 $m^2\ g^{-1}$) and Fe-WS_2@CC (44 $m^2\ g^{-1}$) as shown in **Figure**

3A. The pore size distribution plots from the N_2 adsorption-desorption isotherm of the samples were presented in the **Figure S3, supporting information** and in the inset of Fig. 3A showed the 1T-Fe/P-WS_2@CC has the pore size distribution range approximately from 2

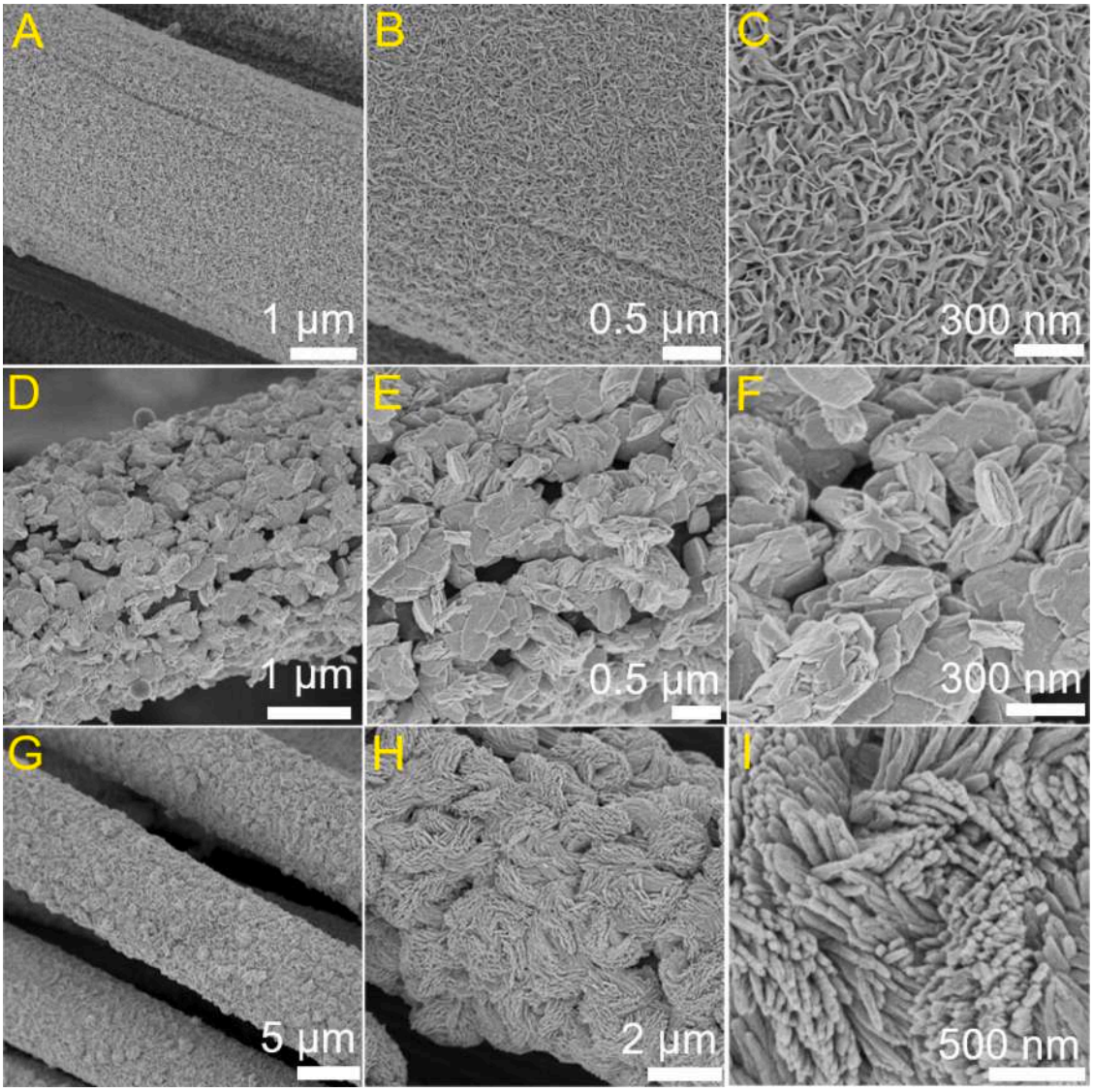

Fig. 2. FE-SEM images of WS_2@CC (A – C), P-WS_2@CC (D – F), and Fe-WS_2@CC (G – I) from lower to higher magnifications.

nm to 50 nm with an average diameter of 24 nm, whereas WS_2@CC shows average pore diameter around 14 nm. For Fe-WS_2@CC the average pore diameter was observed ~ 11 nm and P-WS_2@CC showed the average pore diameter of 32 nm. From these results, we concluded that the 1T-Fe/P-WS_2@CC electrodes are morphologically superior compared to WS_2@CC, Fe-WS_2@CC, and P-WS_2@CC with higher surface area and porosity which enable higher number in active sites and space for electrolyte ions to reacts and pass-through [10]. This improvement in morphology following formation of the agave-leave type 3D-dendritic nanostructures could be attributed to the substitutional doping of Fe and P to form respective crystal lattice, stabilization of the 1T-phase of WS_2 and viable bond formation possibilities between similar and dissimilar elements during the formation of the sheets in bottom up synthesis [28,34].

The crystallographic nature of the 1T-Fe/P-WS_2@CC was inspected by powder X-ray diffraction (PXRD) study, and the pattern is presented in Fig. 3B. The PXRD results showed characteristic peak regarding (002) plane is appeared to a lower region of around 9.4° compared to that of 2H-WS_2 (14.4°), which suggest better crystallinity and proven to be octahedral (1T) enriched structure due to intercalation and doping of Fe and P in the interlayers and in the lattice itself. [18][39] The diffraction peaks at 17.6° and 29° are designated for the planes (004) and (006) of 1T- Fe/P-WS_2@CC and the peaks at 32.45° and 57.44° is identified as (100) and (110) planes of the 1T- Fe/P-WS_2@CC. Overall, the PXRD pattern of Fe/P-WS_2@CC is exactly matching with the previously reported literature of 1T-WS_2 with very little change in the peak position [24,25,35]. Whereas, the controlled PXRD experiments of 2H-WS_2@CC, Fe-WS_2@CC, and P-WS_2@CC show the presence of peak corresponding to (002) plane at 14.36°, 13.98°, and 13.62° respectively (**Figure S4,** supporting information). Other peaks remain in the similar position. This shift in the (002) peak is a clear evidence of the formation of the 1T-phase [18,25].

Raman spectroscopic analysis were also performed to further confirm the chemical fingerprint, polymorphs, phases, and variation in crystallinity of the electrode samples at laser wavelength 532 nm and with a laser power density of 0.2 mW. On examining the Raman spectra shown in Fig. 3**C** collected from WS_2 vertical nanosheets grown on CC substrate, the characteristic Raman modes at 352.5 and 414.8 cm^{-1} are due to the in plane E^1_{2g} and A^1_g vibration modes, respectively indicating the formation of 2H-phase of WS_2 [40]. As to the Fig. 3**D** plotted for Raman vibration modes of P-doped WS_2@CC and Fig. 3**E** for Fe-doped WS_2@CC, less matured Raman active modes in lower frequency regions are observed, which indicates the formation and partial stabilization of the 1T-phase WS_2. The significant strong additional intensity

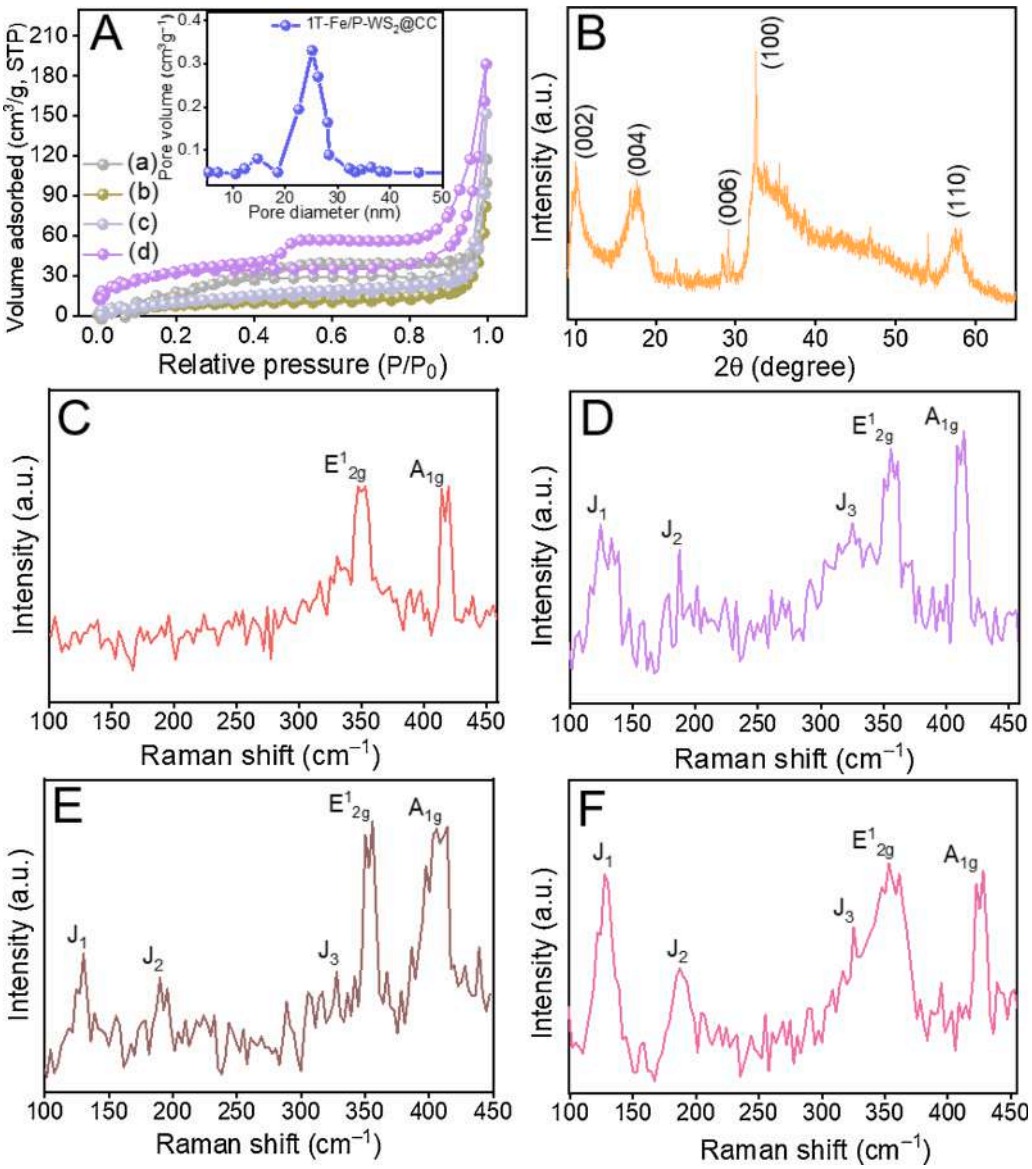

Fig. 3. (A) Nitrogen adsorption- desorption isotherm curves of (a) WS_2@CC (b) P-WS_2@CC (c) Fe-WS_2@CC (d) 1T-Fe/P-WS_2@CC and the BJH pore size distribution curves of 1T-Fe/P-WS_2@CC (inset). (B) Powder X-Ray Diffraction pattern of 1T-Fe/P-WS_2@CC. Raman spectra showing major modes of (C) WS_2, (D) P-WS_2, (E) Fe-WS_2, and (F) 1T- Fe/P-WS_2.

peaks in the lower frequency regions J_1 (131 cm^{-1}), J_2 (188 cm^{-1}), J_3 (325 cm^{-1}) with two prominent peaks E^1_{2g} and A^1_g (Fig. 3F) observed for 1T-Fe/P-WS_2@CC is due to the existence of the zigzag-chain superlattice demonstrating the formation of stable metallic configuration of 1T-Fe/P-WS_2@CC because of Fe and P doping and intercalation [25–41].

To understand the chemical states and composition of elements that exist in 1T-Fe/P-WS_2@CC, X-ray photoelectron spectroscopy (XPS) analysis was conducted and represented in **Figure S5 and** Fig. 4. The full survey spectrum in **Figure S5, supporting information** reveals the presence of W, S, Fe, and P along with trace amount of C and O. The elemental composition is consistent with the results obtained from TEM-EDX (Fig. 1G) or FESEM-EDS spectroscopy (**Figure S1,** supporting information). The core level binding energy peaks at 31.9 and 34.0 eV in the high-resolution XPS spectra of W 4f (Fig. 4A) are due to W $4f_{7/2}$ (W^{4+}) and W $4f_{5/2}$ (W^{4+}) respectively corresponding to 1T-phase and the binding energy peaks at 32.7 eV (W $4f_{7/2}$) and 34.5 eV (W $4f_{5/2}$) are due to 2H-phase of WS_2 as reported in previous study. [25,27,35,38] The peaks intensities for 1T-phase is much higher compared to 2H-phase, clearly indicating the enrichment of 1T-phase for Fe/P-WS_2@CC agave-leave type 3D-dendritic nanostructure. [26] The formation of 1T-Fe/P-WS_2@CC is further supported by the high resolution XPS analysis of S 2p, where the peaks at 161.6 eV (S, 2p3/2) and 162.7 eV (S 2p1/2) corresponding to the octahedral (1T) phase (Fig. 4B) has much higher intensities compared to the intensities obtained from peaks corresponding to 2H-phase i.e., 163.2 eV (S 2p3/2) and 164.6 eV (S 2p1/2) [35,38,41]. The high resolution XPS peaks for Fe 2p (Fig. 4C) appears at 708.5 eV and 710.2 eV (Fe 2p3/2) in the XPS spectra discloses the characteristic signals of Fe^{3+} state and the higher binding energy 713.5 eV (Fe 2p3/2) is attributed to oxide state, generated due to arial surface oxidation of 1T-Fe/P-WS_2@CC post synthesis [42]. In addition, the two principal well-resolved peaks at 128.9 eV and 129.8 eV present in the XPS spectra (Fig. 4D) corresponds to the doublet of P 2p3/2 and P 2p1/2, respectively [30]. The XPS analyses of the controlled samples i.e., WS_2@CC, Fe-WS_2@CC, and P-WS_2@CC were also carried out to conclusively prove the role of Fe and P doping for the formation of 1T-phase. The deconvoluted high resolution peaks of W 4f7/2 (33.08 eV), W 4f5/2 (35.18 eV), S 2p3/2 (162.08 eV), S 2p1/2 (163.28) and S

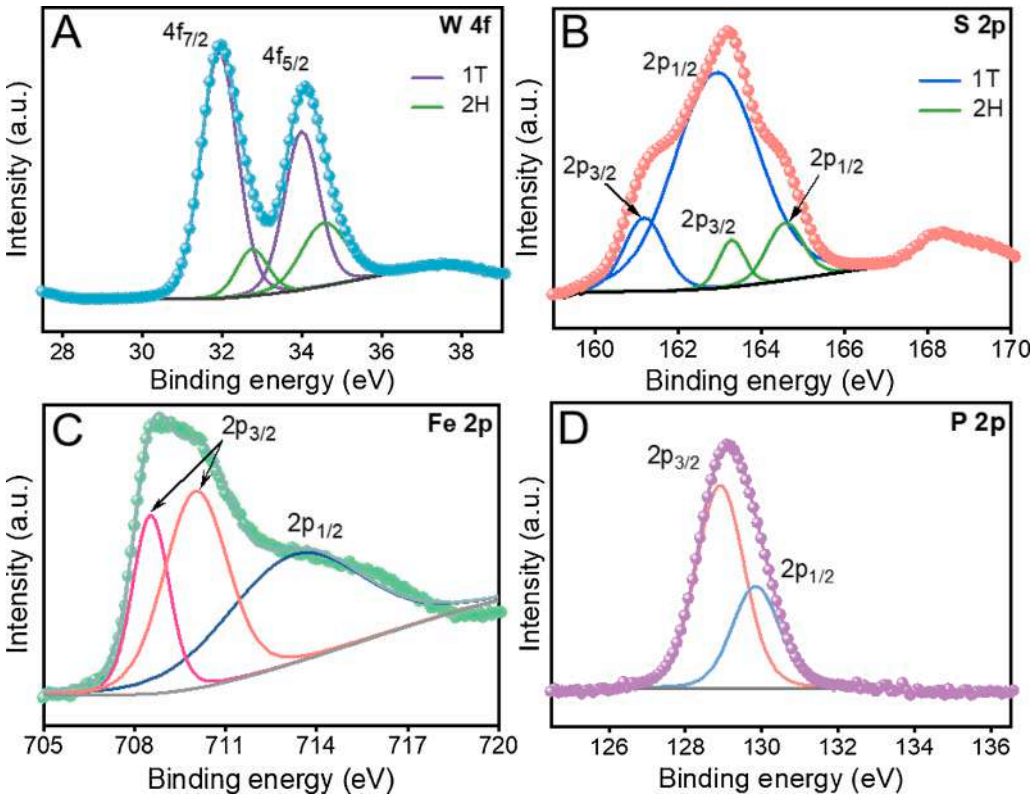

Fig. 4. High resolution XPS spectra for (A) tungsten (W), (B) sulphur (S), (C) iron (Fe), (D) phosphorus (P).

2p5/2 (165.18 eV) for 2H-WS_2@CC in **Figure S6, supporting information** confirmed the formation of the 2H-WS_2. Whereas the deconvoluted high resolution XPS spectra of Fe-WS_2@CC (**Figure S7,** supporting information) and P-WS_2 (**Figure S8,** supporting information) showed predominantly the formation of the 2H-phase along with the additional set of lower binding energy peaks indicating partial stabilization of metallic 1T-phase of WS_2. The above results can prove the formation of Fe/P-WS_2@CC along with enrichment of 1T phase of the same and the important role of the Fe and P doping and intercalation for the stabilization of the 1T-phase. Moreover, as the 1T phase of the WS_2 is stabilized following the doping and intercalation of the Fe and P, it can be concluded along with the atomic resolution TEM images (**Figure S2,** supporting information) that Fe and P is present in the interlayers and lattice, but not adhered on the surface [43]. The ICP-OES result (**Table S1,** supporting information) also shows the significant amount of Fe and P indicating they are mainly present in crystal lattice [16,44].

3.2. Electrochemical characterization

3.2.1. Hydrogen evolution reaction (HER)

The catalytic performance of all the as prepared electrocatalysts for hydrogen evolution reaction (HER) was investigated using saturated Ag/AgCl as reference electrode, graphite rod as counter electrode in a N_2-saturated 1 M KOH electrolyte medium following the conventional three electrode method [44,45]. In general, the adsorption of H_2 on the surface of catalyst is prerequisite of advanced HER catalysts. For this, the HER activity of the samples was investigated by the Linear Sweep Voltammetry (LSV) technique with the potential referenced with hydrogen electrode (RHE). The ohmic drop caused due to the solution resistance was eliminated following iR correction, which was made by using resistivity (R_s) value obtained from EIS curves. For the ease of comparative explanation, the LSV curves for as synthesized 1T-Fe/P-WS_2@CC, Fe-WS_2@CC, P-WS_2@CC, and WS_2@CC as well as bare CC and commercial Pt/C@CC were taken and plotted together in Fig. 5A. The LSV data of 1T-Fe/P-WS_2@CC shows remarkable HER performance with the very low overpotential of 116 mV to achieve the current density of 10 mA cm^{-2} and 180 mV to reach the current density of 50 mA cm^{-2} **(**Fig. 5B**).** The polarization curves in Fig. 5A also shows that the 1T-Fe/P-WS_2@CC has much higher HER-catalytic efficacy than P-WS_2@CC, Fe-WS_2@CC and WS_2@CC is due to enrichment of 1T-phase, activation of the basal planes, lattice distortion and rapid electron transfer in the basal plane in it [16,18,27]. However, as the electrocatalysis performance involving HER and OER mechanism is a complicated process, it is difficult to calculate the contribution of a particular factor or quantitative synergistic involvement of more than one factor. It can also be seen from Fig. 5B, control materials namely, WS_2@CC, P-WS_2@CC and Fe-WS_2@CC showed overpotential (η_{HER}) of 294 mV, 221 mV, and 172 mV respectively to reach the current density of 10 mA cm^{-2} and to achieve current density of 50 mA cm^{-2}, WS_2@CC, P-WS_2@CC, and Fe-WS_2@CC shows overpotential of 325 mV, 293 mV, and 244 mV respectively. The overpotential value of commercial Pt/C electrode was also calculated, and it was observed that Pt/C required an overpotential of 58 mV and 136 mV to reach current density of 10 mA cm^{-2} and 50 mA cm^{-2} respectively **(**Fig. 5A&B**).** Bare CC does not show any significant HER activity (Fig. 5A), thus, contribution of it towards catalytic HER performance of the as synthesized electrode could be considered as negligible. Moreover, the HER kinetics for the rate determining step of hydrogen evolution reaction were investigated by Tafel plots and the Tafel slop values (Fig. 5C) by using Tafel equation; $\eta = a + b \log j$ (b → Tafel slope). The Tafel slop value for 1T-Fe/P-WS_2@CC was found to be lowest (65 mV dec^{-1}) and follows the order WS_2@CC (123 mV dec^{-1}) > P-WS_2@CC (114 mV dec^{-1}) > Fe-WS_2@CC (105 mV dec^{-1}). A higher Tafel slope indicates slow progress of reaction in the electrode and electrolyte interface, which leads to a higher overpotential is due to the requirement of large activation energy to achieve HER. Based on the lower Tafel slop value obtained for 1T-Fe/P-WS_2@CC in alkaline medium the HER is supposed to be processed via Volmer-Heyrovsky mechanism [33]. The Volmer-Heyrovsky mechanism

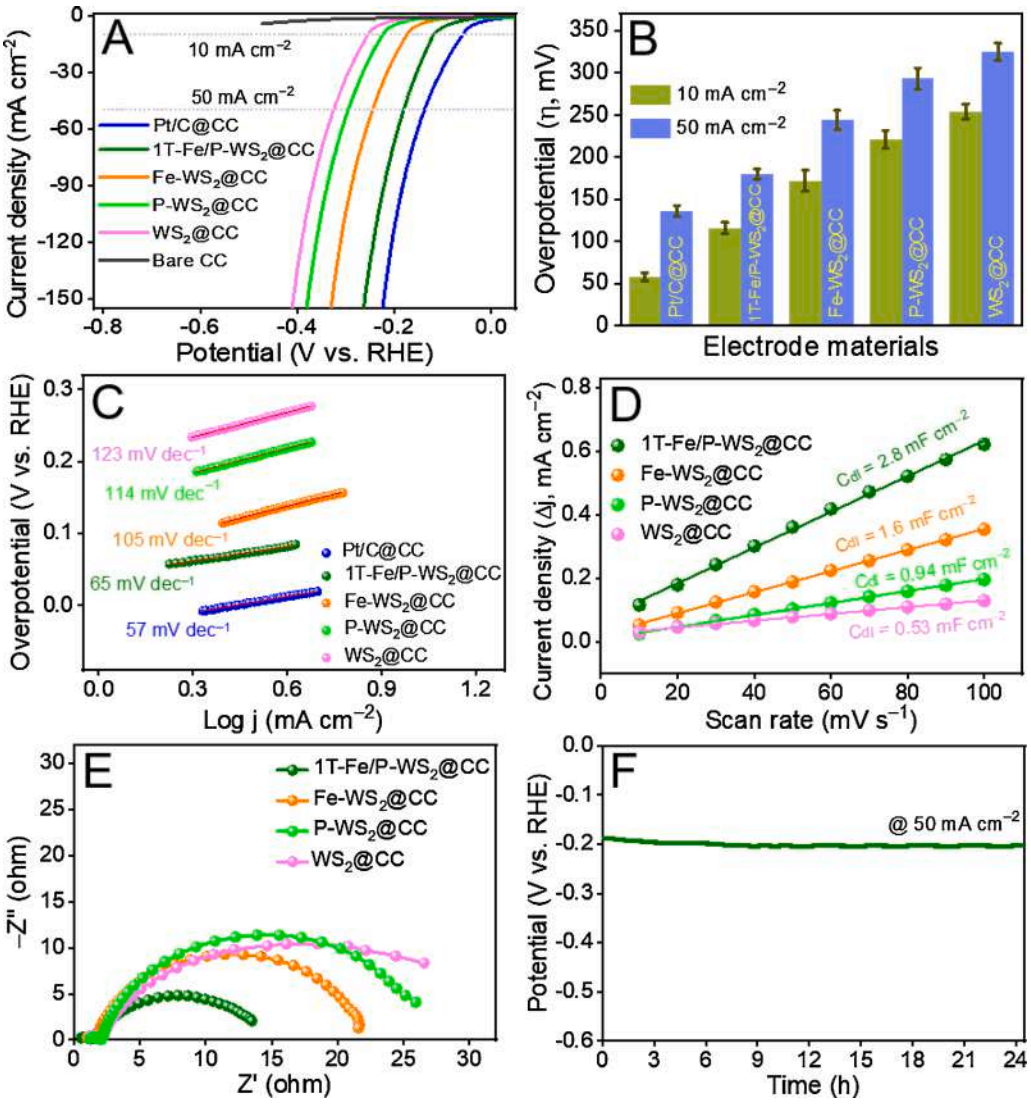

Fig. 5. Electrochemical HER Activity: (A) HER polarization curves after iR correction. (B) Overpotentials of different samples at the current densities of 10 mA cm^{-2} and 50 mA cm^{-2} for HER. (C) Tafel plots and their corresponding Tafel slops. (D) Plots of current density differences (Δj) against scan rates. (E) Nyquist plot for EIS measurements. (F) Chrono-potentiometric stability curve of 1T-Fe/P-WS_2@CC at constant current density 50 mA cm^{-2} for HER activity.

involves the fast discharge reaction of H atom (H*) and OH- ion (Volmer step) and then a rate determining recombination or adsorption reactions (Heyrovsky or Tafel step) outlined as follows:

$$H_2O + e^- \rightarrow H^* + OH^- \text{ (Volmer step)} \quad (5)$$

$$H_2O + e^- + H^* \rightarrow H_2 + OH^- \text{ (Heyrovsky step)} \quad (6)$$

$$H^* + H^* \rightarrow H_2 \text{ (Tafel step)} \quad (7)$$

The enhanced HER kinetics related to the surface chemistry and the electronic structure of the electrode materials are further validated by comparing the electrochemical surface area (ECSA) by measuring the double layer capacitance (**Figure S9,** supporting information and Fig. 5D**).** The highest C_{dl} value 2.8 m F cm^{-2} was observed for 1T-Fe/P-WS_2@CC than other controlled catalysts i.e., Fe-WS_2@CC (C_{dl} = 1.6 m F cm^{-2}), P-WS_2@CC (C_{dl} = 0.94 m F cm^{-2}), and WS_2@CC (C_{dl} = 0.53 m F cm^{-2}) indicates the significant increase of ECSA demonstrating the proliferation of the electroactive sites. The high ECSA value for 1T-Fe/P-WS_2@CC is attributed to the higher BET surface area (Fig. 2A) and porous 3D-dendritic nanostructures as revealed in FE-SEM images (Fig. 1C) obtained following doping of Fe and P. The capacitive behaviors and interfacial nature of electrocatalysts at active state is accessed by electrochemical impedance spectroscopy (EIS) measurements (Fig. 5E). The lowest charge transfer resistance (R_{ct}) was observed for 1T-Fe/P-WS_2@CC than that for other as synthesized intermediate catalysts (Fig. 5E) indicates lower resistance at the electrode-electrolyte interface, which results fast electron transfer kinetics. For sustainable H_2 production and the evaluation of electrocatalyst in commercial applications, the durability test is very important. For this, we projected a chrono-potentiometric long-term stability test of 1T-Fe/P-WS_2@CC under a constant potential of 50 mA cm^{-2} for 24 h (Fig. 5F). The results showed initial potential did not changed significantly throughout the test thus, established superior long-term stability of the 1T-Fe/P-WS_2@CC. The durability test was also carried out following LSV measurement followed by consecutives potential cycling by voltammograms for 1000 CV cycles. LSV characteristics after completion of the durability test also did not deviate sharply (**Figure S10,** supporting information) demonstrating the robustness of 1T-Fe/P-WS_2@CC. Hence, it is noteworthy that, 1T-Fe/P-WS_2@CC works in a stable state in alkaline medium along with high HER-catalytic efficacy (**Table S2,** supporting information) showing the great potential of it as an alternative to the noble metal based electrocatalysts for practical HER applications.

3.2.2. Oxygen evolution reaction (OER)

The OER catalytic performance of the as-prepared electrocatalysts i.e., 1T-Fe/P-WS_2@CC, Fe-WS_2@CC, P-WS_2@CC, and WS_2@CC were also investigated using N_2-saturated 1 M KOH electrolyte, saturated Ag/AgCl reference electrode and graphite rod counter electrode in a conventional three electrode system. We have analyzed the OER efficiency of the as synthesized electrode material by LSV measurement at the scan rate of 2 mV s^{-1} of 1 cm^2 sized electrode as the working electrode. The analysis was carried out after the activation of electrode following conjugative CV cycles. Fig. 6A represents the LSV results after iR correction for 1T-Fe/P-WS_2@CC, Fe-WS_2@CC, P-WS_2@CC, WS_2@CC along with bare CC and commercial RuO_2 deposited on CC for comparison. Overpotentials were calculated using the formula $\eta = E_{RHE} - 1.23$ V (E_{RHE} = potential with respect to reversible hydrogen electrode). Overpotential required to achieve a current densities 10 mA cm^{-2} and 50 mA cm^{-2} are always regarded as the benchmark to compare the OER catalytic efficacy. In this case we found 1T-Fe/P-WS_2@CC exhibits a significantly low overpotential of 267 mV at 10 mA cm^{-2} and 299 mV at 50 mA cm^{-2}, which is much smaller than that of other as synthesized Fe-WS_2@CC, P-WS_2@CC, WS_2@CC, and the commercial materials RuO_2. Fe-WS_2@CC, P-WS_2@CC, WS_2@CC and RuO_2 required an overpotentials of 277, 325, 378, and 284 mV to reach current density of 10 mA cm^{-2} and 327, 414, 489, and 343 mV to reach current density of 50 mA cm^{-2} respectively (Fig. 6B). Further the reaction kinetics in the electrode and electrolyte interface was analyzed by Tafel plots and Tafel slop values as displayed in Fig. 6C. The least Tafel slope value obtained for 1T-Fe/P-WS_2@CC (70.1 mV dec^{-1}) suggests a favorable OER kinetics. The Tafel slope value for commercially used OER catalyst RuO_2@CC was found to be 99.2 mV dec^{-1}, much higher than 1T-Fe/P-WS_2@CC catalyst. Fe-WS_2@CC, P-WS_2@CC and WS_2@CC also showed lower Tafel slope value than 1T-Fe/P-WS_2@CC catalyst (Fig. 6C). The lower Tafel slope and OER-overpotential of 1T-Fe/P-WS_2@CC compared to the other as synthesized intermediate electrocatalysts indicated superior OER-catalytic efficacy which is due to the improvement of the morphology, stabilization of 1T -phase of WS_2, activation of the basal planes following doping of Fe and P and most importantly generation of the additional OER-catalytic sites. The long-term catalytic steadiness and durability of the 1T-Fe/P-WS_2@CC was evaluated by the chrono-potentiometric analysis and consecutive 1000 CV cycles. The chrono-potentiometric stability test for 24 h at an anode current density of 50 mA cm^{-2} showed no significant change in initial potential throughout the test represented in Fig. 6**D** indicating superior stability. Moreover, the LSV measurement before and after chrono-potentiometric stability test and 1000 CV cycles showed no substantial deviation in the LSV curve (**Figure S11**, supporting information) also demonstrate long-term stability of the 1T-Fe/P-WS_2@CC catalyst. Thus, all the above discussion established 1T-Fe/P-WS_2@CC as an efficient OER-catalyst (**Table S3,** supporting information) with long-term stability.

3.2.3. Overall water splitting performance

The excellent electro-catalytic HER and OER performance of the 1T-Fe/P-WS_2@CC has inspired the fabrication of a full-cell water splitting device in two-electrode configurations. For this, 1 × 1 cm^2 size of 1T-Fe/P-WS_2@CC is integrated both as cathode and anode using N_2-saturated 1 M KOH as electrolyte to develop the alkaline electrolyzer (Fig. 7A). The effectiveness of the device towards overall water-splitting was verified by LSV measurement (Fig. 7B). For comparison, we have performed a control experiment using RuO_2 (+) deposited on CC as OER-electrode and Pt/C (−) deposited on CC as HER electrode and bare carbon cloth (+,−) for finding contribution of the current collector. It can be evidently seen from Fig. 7B that the 1T-Fe/P-WS_2@CC (+,−) alkaline electrolyzer showed superior overall electro-catalytic performance with cell voltage of 1.53 V to achieve current density 10 mA cm^{-2}, whereas RuO_2(+)//Pt/C(−) coupled alkaline electrolyzer required cell voltage of 1.57 V to reach current density of 10 mA cm^{-2}. No considerable catalytic efficacy was observed from bare CC (+,−) coupled elctrolyzer. The digital photographs in Fig. 7A showed the as-constructed self-powered overall water splitting system and the schematics for water electrolysis

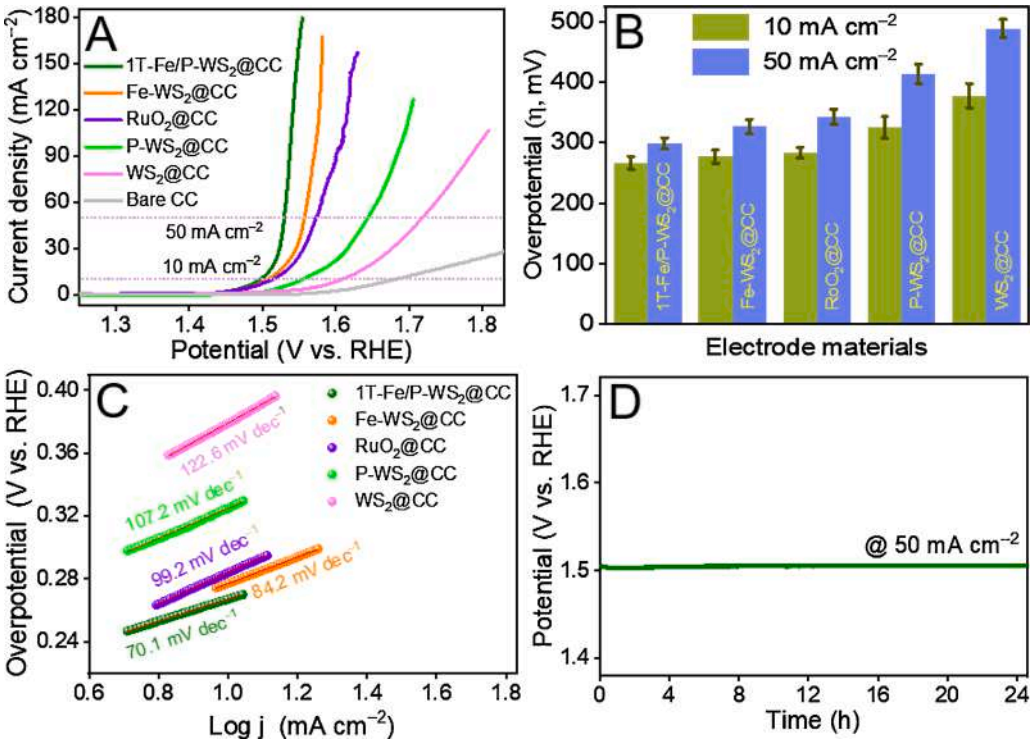

Fig. 6. Electrochemical OER Activity: (A) OER polarization curves after iR correction. (B) Overpotentials of different samples at the current densities of 10 mA cm^{-2} and 50 mA cm^{-2}. (C) Tafel plots and their corresponding Tafel slop. (D) Chrono-potentiometric stability curve of 1T-Fe/P-WS_2@CC at constant current density 50 mA cm^{-2}.

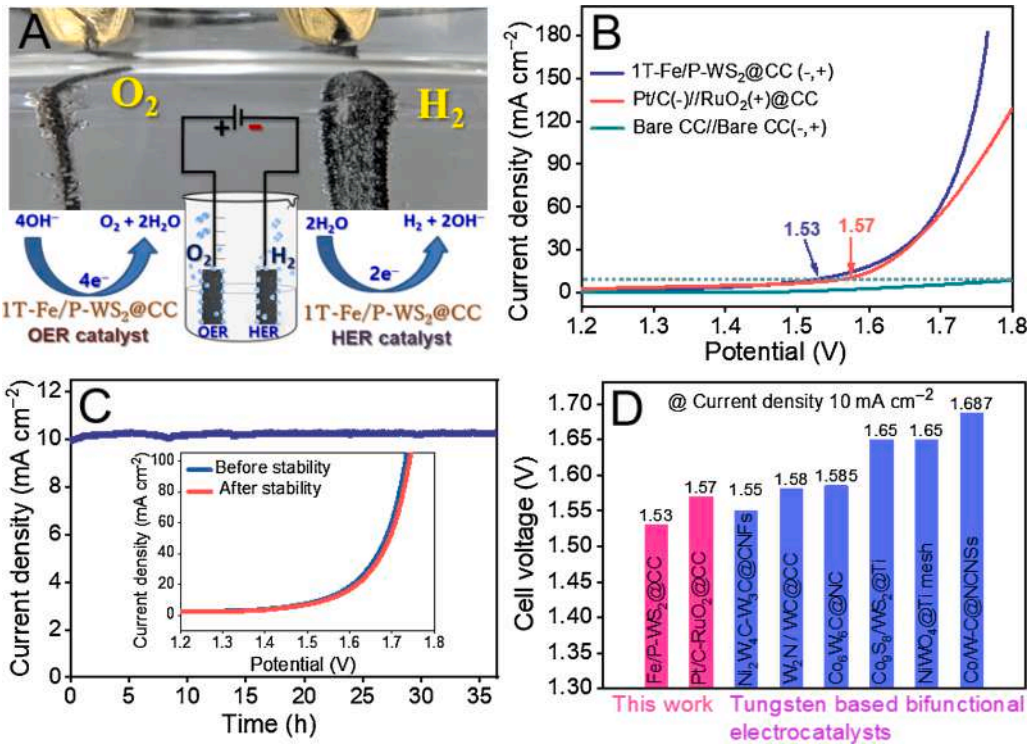

Fig. 7. Overall water splitting device performance: (A) Digital photograph for showing the as-constructed self-powered two electrode overall water splitting system and the schematics for alkaline water electrolysis cell setup. (B) LSV polarization curves of two electrode cell assembled (after iR compensation). (C) Chronoamperometric stability test of 1T-Fe/P-WS_2@CC in alkaline electrolyzer for water splitting device set up (inset; LSV polarization curve before and after stability test of 1T-Fe/P-WS_2@CC electrode). (D) Comparison of cell voltage for water splitting performance of 1T-Fe/P-WS_2@CC with other recently reported electrode devices.

cell setup where surplus amount of H_2 gas bubbles are released towards cathode and the O_2 gas bubbles are released at anode. For the industrial necessity as a potential electrocatalyst and its practical application, a 36 h long-term durability test was conducted for 1T-Fe/P-WS_2@CC (+,−) electrolytic cell by chronoamperometric method (Fig. 7C). During 36 h of continuous electrolysis reaction, the steady state current is recorded with very slight degradation of the initial current density (~ 2%) and the cell voltage similar to that for before durability test (Inset; Fig. 7C) showing the excellent electrochemical stability. Impressively, our bifunctional coupled alkaline electrolyzer for overall water splitting activity is far superior to the recently reported tungsten-based bifunctional electrocatalyst as given in Fig. 7D **and Table S4, supporting information**. The structural toughness of the 1T-Fe/P-WS_2@CC was finally confirmed by FE-SEM and TEM analysis obtained after the chronoamperometric test. The FE-SEM image (**Figure S12A,** supporting information), TEM image (**Figure S12B,** supporting information), and HR-TEM image (**Figure S12C,** supporting information) showed no substantial change in the morphological structure of the catalyst and retain their original structure after long-term stability. Similarly, the STEM and their corresponding elemental mapping post stability test in **Figure S12D-E, supporting information** shows the similar elemental composition. In addition, the Powder XRD patterns for 1T-Fe/P-WS_2@CC after stability test showed no significant changes in the core crystallinity of the1T-Fe/P-WS_2@CC (**Figure S13,** supporting information). Similarly, the HR-XPS peaks of the constituent elements W 4f, S 2p, and Fe 2p did not shift significantly from their original position (**Figure S14,** supporting information), while the deconvoluted P 2p peaks slightly shifted to 132.9 eV (p 2p3/2) and 133.8 eV (p 2p1/2) possibly due to surface oxidation of phosphorus after the stability test of 1T-Fe/P-WS_2@CC. Moreover, the BET surface area analysis of the 1T-Fe/P-WS_2@CC after the stability test also showed similar results with the as-synthesized one (**Figure S15,** supporting information). All these findings established superior ability of 1T-Fe/P-WS_2@CC for overall water-splitting with low cell voltage makes it an ideal candidate for industrial scale catalyst for the production of hydrogen gas at low cost.

4. Conclusion

In summary, we have fabricated 1T-phase enriched 3D-dendritic nanostructures of WS_2 with high surface area and active basal planes following doping of Fe and P on flexible carbon cloth (CC; 1T-Fe/P-WS_2@CC) for efficient overall water splitting. 1T-Fe/P-WS_2@CC shows considerably superior performance with overpotential of 116 mV for HER and 267 mV for OER to drive a current density of 10 mA cm^{-2}, smaller Tafel slope of 65 mV dec^{-1} for HER and 70.1 mV dec^{-1} for OER as well as the excellent long-term stability. The performance of 1T-Fe/P-WS_2@CC is much higher towards both HER and OER compared to the control materials i.e, WS_2@CC, P-WS_2@CC, Fe-WS_2@CC is due to enrichment of 1T-phase, activation of basal plane and formation of superior morphology with high surface area and porosity achieved following doping and intercalation of Fe and P. The 1T-Fe/P-WS_2@CC (+,−) alkaline elctrolyzer also showed superior performance, requires only 1.53 V cell potential to generate a current density of 10 mA cm^{-2} and the performance is comparable with the commercial RuO_2(+)//Pt/C(-) device; even little better at higher potential. Finally, we can conclude that by tuning the structural and intrinsic electronic properties of the WS_2 following proper combination of multiple synergistic effect enabled by simultaneous doping of Fe and P we have fabricated a highly efficient, stable, and commercially viable electrocatalyst for large scale industrial hydrogen production.

Declaration of Competing Interest

The authors declare no conflict of interest.

Acknowledgements

This work was supported by the Basic Science Research Program (2017R1A2B3004917) of National Research Foundation (NRF), Ministry of Science and ICT, Republic of Korea.

Appendix A. Supplementary data

Supplementary material related to this article can be found, in the online version, at doi:https://doi.org/10.1016/j.apcatb.2021.119897.

References

[1] J. Chow, R.J. Kopp, P.R. Portney, Energy resources and global development, Science 302 (2003) 1528–1531, https://doi.org/10.1126/science.1091939.
[2] M.S. Dresselhaus, I.L. Thomas, Alternative energy technologies. dresselhaus2001, Nature 414 (2001) 332–337, https://doi.org/10.1038/35104599.
[3] S. Chu, Y. Cui, N. Liu, The path towards sustainable energy, Nat. Mater. 16 (2016) 16–22, https://doi.org/10.1038/nmat4834.
[4] S. Chu, A. Majumdar, Opportunities and challenges for a sustainable energy future, Nature 488 (2012) 294–303, https://doi.org/10.1038/nature11475.
[5] I. Dincer, C. Zamfirescu, Sustainable hydrogen production, Sustain. Hydrog. Prod. 305 (2016) 1–479, https://doi.org/10.1016/b978-0-444-64203-5.00001-0.
[6] J. Zhu, L. Hu, P. Zhao, L.Y.S. Lee, K.Y. Wong, Recent Advances in Electrocatalytic Hydrogen Evolution Using Nanoparticles, Chem. Rev. 120 (2020) 851–918, https://doi.org/10.1021/acs.chemrev.9b00248.
[7] D.T. Tran, D.C. Nguyen, H.T. Le, T. Kshetri, V.H. Hoa, T.L.L. Doan, N.H. Kim, J. H. Lee, Recent progress on single atom/sub-nano electrocatalysts for energy applications, Prog. Mater. Sci. 115 (2021) 100711, https://doi.org/10.1016/j.pmatsci.2020.100711.
[8] Q. Fu, J. Han, X. Wang, P. Xu, T. Yao, J. Zhong, W. Zhong, S. Liu, T. Gao, Z. Zhang, L. Xu, B. Song, 2D transition metal dichalcogenides: design, modulation, and challenges in electrocatalysis, Adv. Mater. 1907818 (2020) 1–24, https://doi.org/10.1002/adma.201907818.
[9] Z.W. She, J. Kibsgaard, C.F. Dickens, I. Chorkendorff, J.K. Nørskov, T.F. Jaramillo, Combining theory and experiment in electrocatalysis: insights into materials design, Science 355 (2017), https://doi.org/10.1126/science.aad4998.
[10] J. Hou, Y. Wu, B. Zhang, S. Cao, Z. Li, L. Sun, Rational design of nanoarray architectures for electrocatalytic water splitting, Adv. Funct. Mater. 29 (2019) 1–39, https://doi.org/10.1002/adfm.201808367.
[11] J. Kibsgaard, I. Chorkendorff, Considerations for the scaling-up of water splitting catalysts, Nat. Energy 4 (2019) 430–433, https://doi.org/10.1038/s41560-019-0407-1.
[12] Z. Li, W. Niu, Z. Yang, A. Kara, Q. Wang, M. Wang, M. Gu, Z. Feng, Y. Du, Y. Yang, Boosting alkaline hydrogen evolution: the dominating role of interior modification in surface electrocatalysis, Energy Environ. Sci. 13 (2020) 3110–3118, https://doi.org/10.1039/d0ee01750g.
[13] M.S. Sokolikova, C. Mattevi, Direct synthesis of metastable phases of 2D transition metal dichalcogenides, Chem. Soc. Rev. 49 (2020) 3952–3980, https://doi.org/10.1039/d0cs00143k.
[14] P. Luo, F. Zhuge, Q. Zhang, Y. Chen, L. Lv, Y. Huang, H. Li, T. Zhai, Doping engineering and functionalization of two-dimensional metal chalcogenides, Nanoscale Horiz. 4 (2019) 26–51, https://doi.org/10.1039/c8nh00150b.
[15] A.P. Tiwari, D. Kim, Y. Kim, H. Lee, Bifunctional oxygen electrocatalysis through chemical bonding of transition metal chalcogenides on conductive carbons, Adv. Energy Mater. 7 (2017) 1–9, https://doi.org/10.1002/aenm.201602217.
[16] U.N. Pan, T.I. Singh, D.R. Paudel, C.C. Gudal, N.H. Kim, J.H. Lee, Covalent doping of Ni and P on 1T-enriched MoS_2 bifunctional 2D-nanostructures with active basal planes and expanded interlayers boosts electrocatalytic water splitting, J. Mater. Chem. A 5 (2020) 23566–23576, https://doi.org/10.1039/D0TA05865C.
[17] Y. Yang, H. Fei, G. Ruan, C. Xiang, J.M. Tour, Edge-oriented MoS_2 nanoporous films as flexible electrodes for hydrogen evolution reactions and supercapacitor devices, Adv. Mater. 26 (2014) 8163–8168, https://doi.org/10.1002/adma.201402847.
[18] K. Liang, Y. Yan, L. Guo, K. Marcus, Z. Li, L. Zhou, Y. Li, R. Ye, N. Orlovskaya, Y. H. Sohn, Y. Yang, Strained $W(Se_xS_{1-x})_2$ nanoporous films for highly efficient hydrogen evolution, ACS Energy Lett. 2 (2017) 1315–1320, https://doi.org/10.1021/acsenergylett.7b00326.
[19] M.A. Lukowski, A.S. Daniel, C.R. English, F. Meng, A. Forticaux, R.J. Hamers, S. Jin, Highly active hydrogen evolution catalysis from metallic WS_2 nanosheets, Energy Environ. Sci. 7 (2014) 2608–2613, https://doi.org/10.1039/c4ee01329h.
[20] Z. Zhang, P. Chen, X. Duan, K. Zang, J. Luo, X. Duan, Robust epitaxial growth of two-dimensional heterostructures, multiheterostructures, and superlattices, Science 357 (2017) 788–792, https://doi.org/10.1126/science.aan6814.
[21] K. Shiva, H.S.S. Ramakrishna Matte, H.B. Rajendra, A.J. Bhattacharyya, C.N. R. Rao, Employing synergistic interactions between few-layer WS2 and reduced graphene oxide to improve lithium storage, cyclability and rate capability of Li-ion batteries, Nano Energy 2 (2013) 787–793, https://doi.org/10.1016/j.nanoen.2013.02.001.
[22] R.J. Toh, Z. Sofer, J. Luxa, D. Sedmidubský, M. Pumera, 3R phase of MoS_2 and WS_2 outperforms the corresponding 2H phase for hydrogen evolution, Chem. Commun. 53 (2017) 3054–3057, https://doi.org/10.1039/c6cc09952a.
[23] D. Wang, Q. Li, C. Han, Z. Xing, X. Yang, When NiO@Ni Meets WS_2nanosheet array: A highly efficient and ultrastable electrocatalyst for overall water splitting, ACS Cent. Sci. 4 (2018) 112–119, https://doi.org/10.1021/acscentsci.7b00502.
[24] B. Mahler, V. Hoepfner, K. Liao, G.A. Ozin, Colloidal synthesis of 1T-WS_2 and 2H-WS_2 nanosheets: applications for photocatalytic hydrogen evolution, J. Am. Chem. Soc. 136 (2014) 14121–14127, https://doi.org/10.1021/ja506261t.
[25] Q. Liu, X. Li, Z. Xiao, Y. Zhou, H. Chen, A. Khalil, T. Xiang, J. Xu, W. Chu, X. Wu, J. Yang, C. Wang, Y. Xiong, C. Jin, P.M. Ajayan, L. Song, Stable metallic 1T-WS_2 nanoribbons intercalated with Ammonia ions: the correlation between structure and Electrical/Optical properties, Adv. Mater. 27 (2015) 4837–4844, https://doi.org/10.1002/adma.201502134.
[26] X. Zhao, X. Ma, J. Sun, D. Li, X. Yang, Enhanced catalytic activities of surfactant-assisted exfoliated WS_2 nanodots for hydrogen evolution, ACS Nano 10 (2016) 2159–2166, https://doi.org/10.1021/acsnano.5b06653.
[27] D. Voiry, H. Yamaguchi, J. Li, R. Silva, D.C.B. Alves, T. Fujita, M. Chen, T. Asefa, V. B. Shenoy, G. Eda, M. Chhowalla, Enhanced catalytic activity in strained chemically exfoliated WS_2 nanosheets for hydrogen evolution, Nat. Mater. 12 (2013) 850–855, https://doi.org/10.1038/nmat3700.
[28] A. Eftekhari, Tungsten dichalcogenides (WS_2, WSe_2, and WTe_2): materials chemistry and applications, J. Mater. Chem. A 5 (2017) 18299–18325, https://doi.org/10.1039/c7ta04268j.
[29] Y. Yang, X.L. Fan, R. Pan, W.J. Guo, First-principles investigations of transition-metal doped bilayer WS_2, Phys. Chem. Chem. Phys. 18 (2016) 10152–10157, https://doi.org/10.1039/c6cp00701e.
[30] V.H. Hoa, D.T. Tran, D.C. Nguyen, D.H. Kim, N.H. Kim, J.H. Lee, Molybdenum and phosphorous dual doping in cobalt monolayer interfacial assembled cobalt nanowires for efficient overall water splitting, Adv. Funct. Mater. 2002533 (2020) 1–12, https://doi.org/10.1002/adfm.202002533.
[31] T.A. Shifa, F. Wang, K. Liu, Z. Cheng, K. Xu, Z. Wang, X. Zhan, C. Jiang, J. He, Efficient catalysis of hydrogen evolution reaction from $WS_{2(1-x)}P_{2x}$ nanoribbons, Small 13 (2017) 1603706, https://doi.org/10.1002/smll.201603706.
[32] P. Prabhu, V. Jose, J.M. Lee, Design strategies for development of TMD-Based heterostructures in electrochemical energy systems, Matter 2 (2020) 526–553, https://doi.org/10.1016/j.matt.2020.01.001.
[33] D.C. Nguyen, D.T. Tran, T.L.L. Doan, D.H. Kim, N.H. Kim, J.H. Lee, Rational design of Core@shell structured CoS_x@Cu_2MoS_4 hybridized MoS_2/N,S-Codoped graphene as advanced electrocatalyst for water splitting and Zn-Air battery, Adv. Energy Mater. 10 (2020), https://doi.org/10.1002/aenm.201903289.
[34] U.N. Pan, V. Sharma, T. Kshetri, T.I. Singh, D.R. Paudel, N.H. Kim, J.H. Lee, Freestanding 1T-$Mn_xMo_{1-x}S_{2-y}Se_y$ and $MoFe_2S_{4-z}Se_z$ ultrathin nanosheet-structured electrodes for highly efficient flexible solid-state asymmetric supercapacitors, Small 16 (2020) 4–15, https://doi.org/10.1002/smll.202001691.
[35] W. Ding, L. Hu, J. Dai, X. Tang, R. Wei, Z. Sheng, C. Liang, D. Shao, W. Song, Q. Liu, M. Chen, X. Zhu, S. Chou, X. Zhu, Q. Chen, Y. Sun, S.X. Dou, Highly ambient-stable 1T-MoS_2 and 1T-WS_2 by hydrothermal synthesis under high magnetic fields, ACS Nano 13 (2019) 1694–1702, https://doi.org/10.1021/acsnano.8b07744.
[36] X. Shi, M. Fields, J. Park, J.M. McEnaney, H. Yan, Y. Zhang, C. Tsai, T.F. Jaramillo, R. Sinclair, J.K. Nørskov, X. Zheng, Rapid flame doping of Co to WS_2 for efficient hydrogen evolution, Energy Environ. Sci. 11 (2018) 2270–2277, https://doi.org/10.1039/c8ee01111g.
[37] N. Lee, I.Y. Choi, K.Y. Doh, J. Kim, H. Sim, D. Lee, S.Y. Choi, J.K. Kim, Enhanced catalytic activity of edge-exposed 1T phase WS_2 grown directly on a WO_3 nanohelical array for water splitting, J. Mater. Chem. A 7 (2019) 26378–26384, https://doi.org/10.1039/c9ta07926b.
[38] H.U. Kim, V. Kanade, M. Kim, K.S. Kim, B.S. An, H. Seok, H. Yoo, L.E. Chaney, S. Il Kim, C.W. Yang, G.Y. Yeom, D. Whang, J.H. Lee, T. Kim, Wafer-scale and low-temperature growth of 1T-WS_2 film for efficient and stable hydrogen evolution reaction, Small 16 (2020) 1–7, https://doi.org/10.1002/smll.201905000.
[39] X.J. Chua, J. Luxa, A.Y.S. Eng, S.M. Tan, Z. Sofer, M. Pumera, Negative electrocatalytic effects of p-Doping niobium and tantalum on MoS_2 and WS_2 for the hydrogen evolution reaction and oxygen reduction reaction, ACS Catal. 6 (2016) 5724–5734, https://doi.org/10.1021/acscatal.6b01593.
[40] A. Berkdemir, H.R. Gutiérrez, A.R. Botello-Méndez, N. Perea-López, A.L. Elías, C. I. Chia, B. Wang, V.H. Crespi, F. López-Urías, J.C. Charlier, H. Terrones, M. Terrones, Identification of individual and few layers of WS_2 using Raman Spectroscopy, Sci. Rep. 3 (2013) 1–8, https://doi.org/10.1038/srep01755.
[41] Q. He, W. Xu, S. Chen, D. Liu, M. Habib, Q. Liu, C. Wang, Y.A. Haleem, T. Xiang, C. Wu, A. Khalil, Q. Fang, Z. Niu, L. Song, In situ growth of metallic 1T-WS_2 nanoislands on single-walled carbon nanotube films for improved electrochemical performance, RSC Adv. 6 (2016) 87919–87925, https://doi.org/10.1039/c6ra19680b.
[42] T.I. Singh, G. Rajeshkhanna, S.B. Singh, T. Kshetri, N.H. Kim, J.H. Lee, Metal–organic framework-derived Fe/Co-based bifunctional electrode for H_2 production through water and urea electrolysis, ChemSusChem. 12 (2019) 4810–4823, https://doi.org/10.1002/cssc.201902232.
[43] Y.C. Lin, C.H. Yeh, H.C. Lin, M.D. Siao, Z. Liu, H. Nakajima, T. Okazaki, M.Y. Chou, K. Suenaga, P.W. Chiu, Stable 1T tungsten disulfide monolayer and Its Junctions: growth and atomic structures, ACS Nano 12 (2018) 12080–12088, https://doi.org/10.1021/acsnano.8b04979.
[44] S. Prabhakaran, J. Balamurugan, N.H. Kim, J.H. Lee, Hierarchical 3D oxygenated cobalt molybdenum selenide nanosheets as robust trifunctional catalyst for water splitting and zinc–Air batteries, Small 16 (2020) 1–13, https://doi.org/10.1002/smll.202000797.
[45] J. Balamurugan, T.T. Nguyen, V. Aravindan, N.H. Kim, J.H. Lee, Highly reversible water splitting cell building from hierarchical 3D nickel manganese oxyphosphide nanosheets, Nano Energy 69 (2020) 104432, https://doi.org/10.1016/j.nanoen.2019.104432.